

## Supplementary Information

### 1. Decaying length of evanescent waves

The extension of evanescent waves, defined as the decaying length to  $1/e$ , is expressed as<sup>1</sup>

$$\delta = (\|k_{az}\|)^{-1} = \frac{1}{k_0 \sqrt{\varepsilon_p \sin^2 \theta_{inc} - \varepsilon_a}}. \quad (S1)$$

The calculation curve in Fig. S1 indicates that the interlayer limits the extension and attenuation of evanescent waves due to its deep-subwavelength thickness.

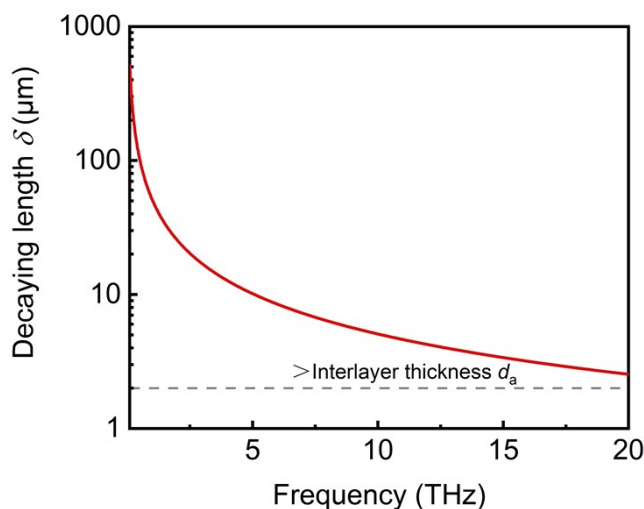


**Fig. S1** Decaying length of evanescent waves as a function of frequency. The decaying length  $\delta$  is always larger than the interlayer thickness within the operating range.

### 2. Transfer matrix method (TMM)

The THz wave propagations through this multilayer stacked system can be numerically simulated by the TMM.<sup>2</sup> Under the condition of transverse magnetic (TM) polarization incidence, it is feasible to describe this structure by the  $2 \times 2$  transfer matrix  $M = D_{p \rightarrow a} P_a(d_a) D_{a \rightarrow s}$ , (S2.1)

where, p, a, and s correspond to prism, air interlayer, and substrate, separately. The transmission matrix  $D_{p \rightarrow a}$ ,  $D_{a \rightarrow s}$  and propagation matrix  $P_a(d_a)$  can be written respectively as

$$D_{p \rightarrow a} = \frac{1}{2} \begin{bmatrix} 1 + \eta_{pa} & 1 - \eta_{pa} \\ 1 - \eta_{pa} & 1 + \eta_{pa} \end{bmatrix}, \quad (S2.2)$$

$$P_a(d_a) = \begin{bmatrix} e^{-ik_{az}d_a} & 0 \\ 0 & e^{ik_{az}d_a} \end{bmatrix}, \quad (S2.3)$$

$$D_{a \rightarrow s} = \frac{1}{2} \begin{bmatrix} 1 + \eta_{as} + \zeta_{as} & 1 - \eta_{ab} - \zeta_{as} \\ 1 - \eta_{as} + \zeta_{as} & 1 + \eta_{ab} - \zeta_{as} \end{bmatrix}. \quad (S2.4)$$

Here, the parameters  $\eta_{pa} = \varepsilon_p k_{az} / \varepsilon_a k_{pz}$ ,  $\eta_{as} = \varepsilon_a k_{sz} / \varepsilon_s k_{az}$ ,  $\zeta_{as} = \sigma k_{sz} / \varepsilon_0 \varepsilon_s \omega$ , where  $\sigma$  is the

conductivity of MoS<sub>2</sub>,  $k_{iz}$  ( $i = p, a, s$ ) =  $k_0 \sqrt{\varepsilon_i - \varepsilon_p \sin^2 \theta_{inc}}$  is the z component of each wave vector under the condition of prism incidence, and  $k_0 = \omega/c$  is the wave vector in the vacuum. Because the transmission channel is closed under ATR conditions, we can easily obtain the absorption spectra and reflection phase for this structure as

$$A = 1 - |r|^2 = 1 - \left| \frac{M_{21}}{M_{11}} \right|^2, \quad (\text{S2.5})$$

$$\phi = \arg(r). \quad (\text{S2.6})$$

The numerical calculation and simulation results are compared, as shown in Fig. S2. These results have a good fit, so we use TMM to improve the research efficiency.

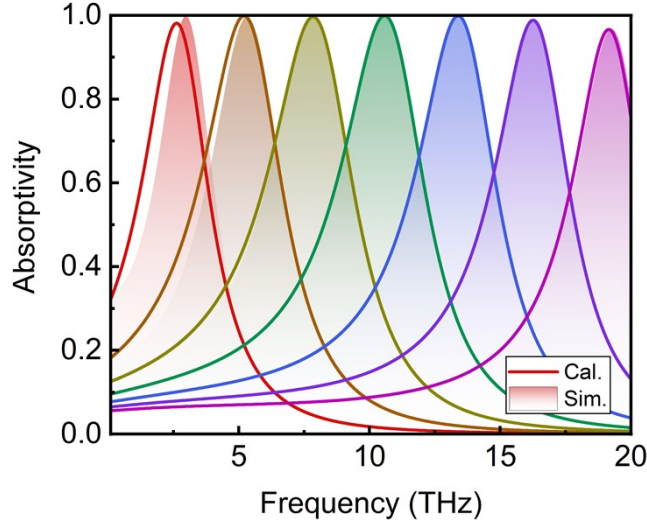


**Fig. S2** TMM calculation (cal.) and COMSOL simulation (sim.) results of absorption with varying carrier concentration  $n$  of MoS<sub>2</sub> from  $1 \times 10^{15}$  to  $7 \times 10^{15}$  cm<sup>-2</sup>.

### 3. Temporal coupled mode theory (TCMT)

Under such ATR conditions, i.e.,  $\theta_{inc} > \arcsin(\varepsilon_s^{1/2} / \varepsilon_p^{1/2})$ , this absorber can be seen as a one-port single-mode system, and the coupled mode equations are described as<sup>3, 4</sup>

$$\frac{da}{dt} = -(if_0 + \gamma_r + \gamma_d)a + \sqrt{2\gamma_r}S_+ = -ifa, \quad (\text{S3.1})$$

$$S_- = \sqrt{2\gamma_r}a - S_+, \quad (\text{S3.2})$$

where  $f_0$  is the resonant frequency,  $\gamma_r$  and  $\gamma_d$  are the radiative leakage rate and intrinsic dissipative rate,  $a$  is the resonant amplitude of the resonance, and  $S_+$  ( $S_-$ ) represents the incident (outgoing) waves. Furthermore, the reflection coefficient and absorptivity can be derived as

$$r = \frac{S_-}{S_+} = -1 + \frac{2\gamma_r}{-i(f - f_0) + \gamma_r + \gamma_d}, \quad (\text{S3.3})$$

$$A = 1 - \left| \frac{S_-}{S_+} \right|^2 = \frac{4\gamma_r\gamma_d}{(f - f_0)^2 + (\gamma_r + \gamma_d)^2}, \quad (\text{S3.4})$$

The maximum absorption  $A_{max}$  at resonant frequency  $f_0$ ,  $Q$ -factor of resonant peak, and the abrupt phase variation can be calculated as

$$A_{\max} = \frac{4\gamma_r\gamma_d}{(\gamma_r + \gamma_d)^2}, \quad (\text{S3.5})$$

$$Q = \frac{f_0}{2(\gamma_r + \gamma_d)}, \quad (\text{S3.6})$$

$$\Delta\phi = \text{angle}\left(\frac{if_{0-} + \gamma_r - \gamma_d}{-if_{0-} + \gamma_r + \gamma_d}\right) - \text{angle}\left(\frac{if_{0+} + \gamma_r - \gamma_d}{-if_{0+} + \gamma_r + \gamma_d}\right). \quad (\text{S3.7})$$

According to these equations, there exists three cases:

- (i) Critical coupling state, i.e.,  $\gamma_r = \gamma_d$ ,  $\Delta\phi = \pi$ . In such case, the unity absorption ( $A = 100\%$ ) can be obtained at the resonant frequency, and the position of resonant frequency is called as phase singularity due to the transformation of phase lineshape.
- (ii) Overdamped state, i.e.,  $\gamma_r < \gamma_d$ ,  $\Delta\phi = 0 : \pi$ . In such case, the absorptivity  $A < 100\%$ .
- (iii) Underdamped state, i.e.,  $\gamma_r > \gamma_d$ ,  $\Delta\phi = \pi : 2\pi$ . In such case, similarly, the absorptivity  $A < 100\%$ .

Additionally, the radiative and dissipative  $Q$ -factors, i.e.,  $Q_r = \frac{f_0}{2\gamma_r}$  and  $Q_d = \frac{f_0}{2\gamma_d}$ , are shown in Fig. S3. So, the  $Q$ -factor of resonant peak can also be described as

$$Q = \frac{Q_r Q_d}{Q_r + Q_d}. \quad (\text{S3.8})$$

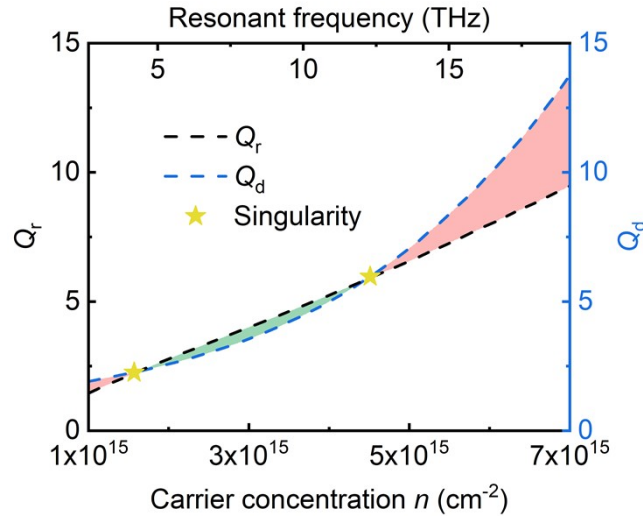


**Fig. S3**  $Q_r$  and  $Q_d$  as functions of carrier concentration  $n$  and resonant frequency  $f_0$ . The intersection points of curves, i.e., singularities, are marked with yellow stars.

In practice, we first calculate the variation of absorptivity  $A$  and reflection phase  $\phi$  through TMM, and then judge the coupled state of the absorption system, while these radiative and dissipative parameters are extracted by the equation (S3.5) and (S3.6). Mutual verifications are conducted using the above numerical calculations and finite element method (FEM) software simulations with COMSOL Multiphysics 5.5.

#### 4. Discussion on angle of polarization or incidence

Under the condition of transverse electrical (TE) polarization incidence, the transmission matrix of TMM that relates the electric fields at the two sides of the air

interlayer/substrate interface could be obtained as<sup>2</sup>

$$D_{a \rightarrow s} = \frac{1}{2} \begin{bmatrix} 1 + \eta_{as} + \zeta_{as} & 1 - \eta_{ab} + \zeta_{as} \\ 1 - \eta_{as} - \zeta_{as} & 1 + \eta_{ab} - \zeta_{as} \end{bmatrix}. \quad (\text{S3.9})$$

The parameters  $\eta_{pa} = k_{az}/k_{pz}$ ,  $\eta_{as} = k_{sz}/k_{az}$ ,  $\zeta_{as} = \sigma\mu_0\omega/k_{az}$  are considered, where  $\mu_0$  is the vacuum permeability. As Fig. S4 shows, the resonant features of plasmon modes cannot be excited by the TE wave incidence in the proposed absorber. Most THz waves are directly reflected by the prism.

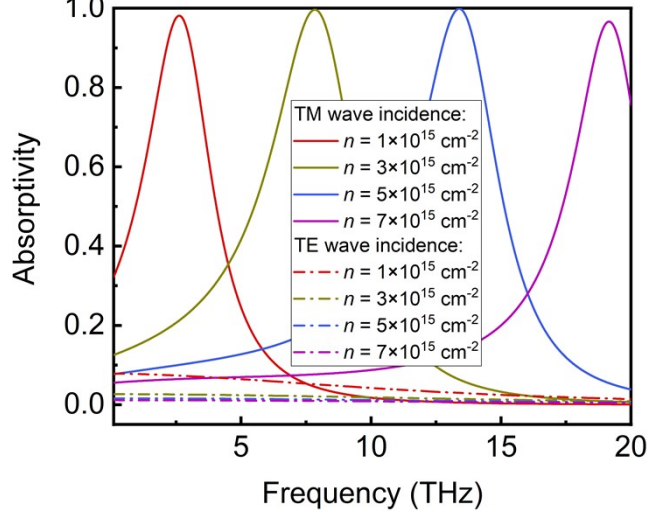


**Fig. S4** Absorption spectra under conditions of TM and TE wave incidence when  $n = 1 \times 10^{15}$ ,  $3 \times 10^{15}$ ,  $5 \times 10^{15}$ , and  $7 \times 10^{15} \text{ cm}^{-2}$ .

The impact of a change in incident angle is calculated as shown in Fig. S5. The resonant features of plasmon modes cannot be generated with non-total internal reflection conditions. For incidence beyond the critical angle, area variations of absorption follow our theoretical analysis of perturbed MoS<sub>2</sub> plasmon modes. It is foreseeable that the similar frequency-agility in this absorption system with single variable of incident angle, but limited incident range constrains the ultra-broadband absorption modulation in the THz regions.

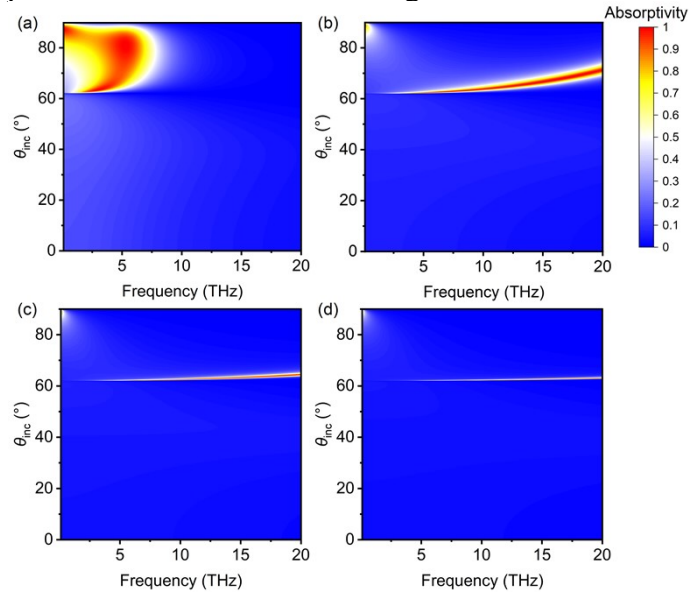


**Fig. S5** Absorption heatmap as functions of frequency and incident angle  $\theta_{inc}$  when (a)  $n = 1 \times 10^{15}$ ,

(b)  $3 \times 10^{15}$ , (c)  $5 \times 10^{15}$ , and (d)  $7 \times 10^{15} \text{ cm}^{-2}$ .

## 5. Discussion on polarization conversion

We evaluate the polarization-sensitive performance of device's reflection with polarization conversion rate (PCR) as shown in Fig. S6. The PCR can be expressed as<sup>5</sup>

$$\text{PCR} = \frac{r_{xy}^2}{r_{xy}^2 + r_{yy}^2}, \quad (\text{S3.10})$$

where  $r_{xy}$  and  $r_{yy}$  are the cross-polarized and the co-polarized reflection coefficients, respectively, which can be modeled as the imaginary and real part of reflection coefficient for p-polarization wave (TM wave) incidence in TMM. The transition of coupling state can also be observed from the change of PCR lineshape in Fig. S6. What's more, the potential polarization modulation and broadband polarization conversion performance is worth noting in this absorption system.

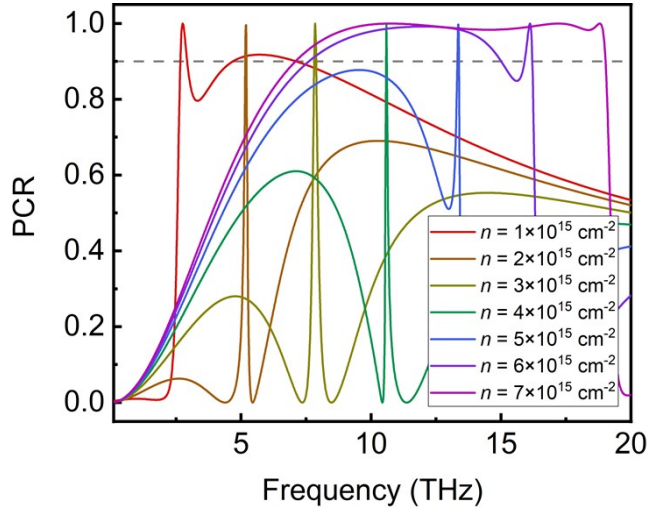


Fig. S6 PCR spectra with varying  $n$  of  $\text{MoS}_2$  from  $1 \times 10^{15}$  to  $7 \times 10^{15} \text{ cm}^{-2}$ .

## 6. Experimental feasibility

The previous literature has experimentally confirmed that large-area  $\text{MoS}_2$  can be evenly manufactured through an improved chemical vapor deposition (CVD) synthetic method and subsequently transferred onto the  $\text{MgF}_2$  substrate<sup>6</sup>. Ionic gating regulation makes it possible to achieve high carrier concentrations. The positive electrode of adjustable power source is in contact with room temperature ionic liquids covered on  $\text{MoS}_2$ , and the negative one is grounded. A high precision translation stage can drive the  $\text{MoS}_2$ -substrate to control the parallel space between prism bottom and  $\text{MoS}_2$  film<sup>7</sup>. Terahertz time-domain spectroscopy (THz-TDS) system is used for generating and receiving THz waves. Nevertheless, this absorber is sensitive to the carrier concentration, interlayer, and incident angle, which possibly limits its stability and practicability. This experimental scheme is expected to be improved and validated in the future.

## 7. Performance comparison

We highlight the performance of the proposed THz absorber by comparing available data from several representative references ever reported, including relative

tuning range ( $W_{\text{RTR}}$ ), approaches, external stimuli, and switching speed in the Table S1. Compared with various approaches, including concurrent control, our work has advantages in tuning range and switching speed.

**Table S1. Performance comparisons with other THz absorbers**

References	$W_{\text{RTR}}$ (%)	Approaches	External stimuli	Switching speed
[8]	107	Liquid metals	Filling liquids	Slow
[9]	69	BP/VO <sub>2</sub>	Doping/thermal	Slow
[10]	200	Graphene/VO <sub>2</sub>	Electrical/thermal	Medium
[11]	85.7	Silicon	Optical pumping	Fast
[12]	79.4	Graphene	Magnetic field	Fast
[13]	76	MoS <sub>2</sub>	Electrical	Fast
This work	175.4	MoS <sub>2</sub>	Electrical	Fast

## References

1. H. Yao and S. Zhong, *Optics Express*, 2014, **22**, 25149-25160.
2. T. Zhan, X. Shi, Y. Dai, X. Liu and J. Zi, *Journal of Physics: Condensed Matter*, 2013, **25**, 215301.
3. J. Nong, L. Tang, G. Lan, P. Luo, C. Guo, J. Yi and W. Wei, *Nanophotonics*, 2020, **9**, 645-655.
4. W. Yin, Z. Shen, S. Li, Y. Cui, F. Gao, H. Hao, L. Zhang and X. Chen, *Optics Express*, 2022, **30**, 32162-32173.
5. S. Liao, J. Sui and H. Zhang, *Optics Express*, 2022, **30**, 34172-34187.
6. Y. Xia, X. Chen, J. Wei, S. Wang, S. Chen, S. Wu, M. Ji, Z. Sun, Z. Xu, W. Bao and P. Zhou, *Nature Materials*, 2023, DOI: 10.1038/s41563-023-01671-5.
7. Y. Huang, S. Zhong, T. Shi, Y.-C. Shen and D. Cui, *Optics Express*, 2019, **27**, 25647-25655.
8. H.-F. Zhang, Z.-L. Wang, C.-X. Hu and H.-B. Liu, *Results in Physics*, 2020, **16**, 102937.
9. T. Wang, L. Qu, L. Qu, Y. Zhang, H. Zhang and M. Cao, *Journal of Physics D: Applied Physics*, 2020, **53**, 145105.
10. Q. Z. Wang, S. Y. Liu, G. J. Ren, H. W. Zhang, S. C. Liu and J. Q. Yao, *Optics Communications*, 2021, **494**, 127050.
11. X. Zhao, Y. Wang, J. Schalch, G. Duan, K. Cremin, J. Zhang, C. Chen, R. D. Averitt and X. Zhang, *ACS Photonics*, 2019, **6**, 830-837.
12. Z. Wei, Y. Jiang and J. Wang, *Crystals*, 2023, **13**, 553.
13. Y. Zhong, Y. Huang, S. Zhong, T. Lin, M. Luo, Y. Shen and J. Ding, *Optical Materials*, 2021, **114**, 110996.